Available online at www.sciencedirect.com
SCIENCE DIRECT®
International Journal of Heat and Fluid Flow 25 (2004) 513–527
International Journal of HEAT AND FLUID FLOW
www.elsevier.com/locate/ijhff

Toward the simulation of complex 3D shear flows using unsteady statistical turbulence models

Joongcheol Paik, Liang Ge, Fotis Sotiropoulos *

School of Civil and Environmental Engineering, Georgia Institute of Technology, 790 Atlantic Drive, Atlanta, GA 30332-0355, USA

Abstract

Recent progress in the numerical simulation of complex, 3D incompressible flows with unsteady statistical turbulence models is reviewed. A second-order accurate, overset grid, numerical method is developed for carrying out unsteady Reynolds-averaged Navier–Stokes (URANS) and detached-eddy simulations (DES) of flows in complex multi-connected domains. Results are reported for three test cases: (1) flow in a channel with four bottom-mounted rectangular piers; (2) flow in a channel with a corner-mounted rectangular block; and (3) flow in a strongly curved rectangular bend. Comparisons between the computed results and laboratory measurements and flow visualization experiments lead to the conclusion that even relatively simple turbulence closure models (such as the standard k–ε model or the one-equation Spalart–Allmaras model) can simulate complex, 3D flows dominated by geometry-induced, large-scale instabilities and unsteady coherent structures with reasonable accuracy. The results for the curved duct case further show that exciting and resolving directly with unsteady statistical turbulence models the low-frequency, large-scale, vortical rolls in a concave wall boundary layer is critical prerequisite for simulating the dramatic effects of concave curvature on the structure of turbulence.

Keywords: Unsteady RANS; DES; Overset grids; 3D separation; Concave wall turbulence

1. Introduction

Most flows of engineering relevance take place in complex, multi-connected domains and are dominated by large-scale unsteadiness and coherent vortex shedding. Unsteady statistical turbulence models constitute the only feasible modeling framework for quantitatively accurate predictions of such flows at real-life Reynolds numbers (Spalart, 2000). Such models include unsteady Reynolds-averaged Navier–Stokes (URANS) and hybrid URANS/LES formulations. Turbulence models in the former category solve the RANS and turbulence closure equations in a time-accurate fashion and thus resolve directly contributions to the time-averaged Reynolds stresses from large-scale, low-frequency deterministic fluctuations in the flow. Therefore, URANS models would in principle work well in flows in which slowly varying coherent structures contribute a considerable portion of the total turbulence kinetic energy (Durbin, 1995; Spalart, 2000). Hybrid modeling strategies are essentially LES models designed to asymptote to a URANS model near solid walls. Such models exploit the ability of LES to resolve all turbulent scales larger than the grid spacing in the bulk of the flow domain while requiring only relatively modest computational resources, which are comparable to those required in a URANS simulation (see Spalart, 2000, for a detailed discussion). A very popular hybrid approach is the so-called Detached-Eddy Simulation (DES), which was proposed by Spalart et al. (1997) and has recently attracted considerable attention due to its simplicity and preliminary success in various complex, massively separated flows. The standard DES model employs a generalized version of the Spalart–Allmaras (SA), one-equation, eddy-viscosity model (Spalart and Allmaras, 1994). The turbulence length scale in the DES model is dependent on the distance from the wall. Sufficiently close to the wall the length scale is set equal to the distance from the wall and the model operates in a URANS mode while far from the wall the length scale is proportional to the local grid spacing and the model switches to the LES mode.

* Corresponding author. Tel.: +1-404-894-4432; fax: +1-404-385-1131.
E-mail address: fs30@ce.gatech.edu (F. Sotiropoulos).

0142-727X/$ - see front matter © 2004 Elsevier Inc. All rights reserved.
doi:10.1016/j.ijheatfluidflow.2004.02.002

Hedges et al. (2002) used URANS and DES to study the flow around a generic airliner landing-gear truck. Squires et al. (2002) and Morton et al. (2003) performed DES of massively separated flows induced by geometrically complex aircrafts. Schmidt and Thiele (2002), Constantinescu et al. (2003) and Iaccarino et al. (2003) carried out URANS and DES for flows past cubes and spheres and compared their predictions with experiments and LES computations. A DES model based on Mentor's SST (shear stress transport) model was also investigated in Strelets (2001) and Hamed et al. (2003). In all these studies DES proved itself superior to URANS for predicting highly energetic three-dimensional turbulent flow features characterized by massive separation and intense vortex shedding. On the other hand, it is notable that URANS performed almost as well as LES and DES in so far as the prediction of time-averaged quantities is concerned.

In this paper we review our recent progress in the application of URANS and DES models to a broad range of 3D, incompressible flows. Unlike previous studies, which focused exclusively on external and for the most part compressible flows, in this work we explore the predictive capabilities of unsteady statistical turbulence models in complex internal incompressible flows. To simulate arbitrarily complex geometries, we develop a domain decomposition method with overset (Chimera) grids. The governing equations are discretized on a non-staggered grid using a second-order accurate finite-volume scheme. Time-accurate solutions are obtained via a second-order accurate, dual-time stepping, artificial compressibility method. URANS and/or DES are carried out for three three-dimensional flow cases, which exhibit rich large-scale dynamics and are dominated by geometry-induced shedding of coherent vortices. The first case is flow in a rectangular open channel with four, bottom-mounted rectangular piers located one behind the other along the flow direction (see Fig. 1). The geometry is further complicated by a rectangular concrete slab connecting the two middle piers, which, as shown in Fig. 1, does not extend all the way to the channel bottom. This configuration is the actual foundation geometry of a bridge over the Chattahoochee River in southern Georgia, USA. URANS computations are carried out for this case using the standard k–ε model with wall functions and calculated mean velocity profiles are compared with measurements. The second test case is flow in the vicinity of a rectangular block attached in the junction region between the side and bottom walls of a rectangular open channel as shown in Fig. 6. URANS, with the SA turbulence model, and DES are carried out for this flow and the results are compared with flow visualization experiments. The final case is flow in a strongly curved rectangular duct. In spite of its geometric simplicity relative to the two other test cases, this case is of great fundamental importance. We seek to explore whether unsteady statistical turbulence models can predict the growth of large-scale coherent rolls inside the centrifugally unstable boundary layer on the concave side of the bend. Such rolls have been documented in experimental investigations of concave wall boundary layers and their action has been linked to the well known dramatic destabilizing effects of concave curvature on the structure of turbulence (Barlow and Johnston, 1988; Patel and Sotiropoulos, 1997). Both DES and URANS with the SA turbulence model are carried for this case and the results are compared with experimental measurements.

2. Numerical method

We solve the 3D, incompressible, URANS and turbulence closure equations formulated in generalized,

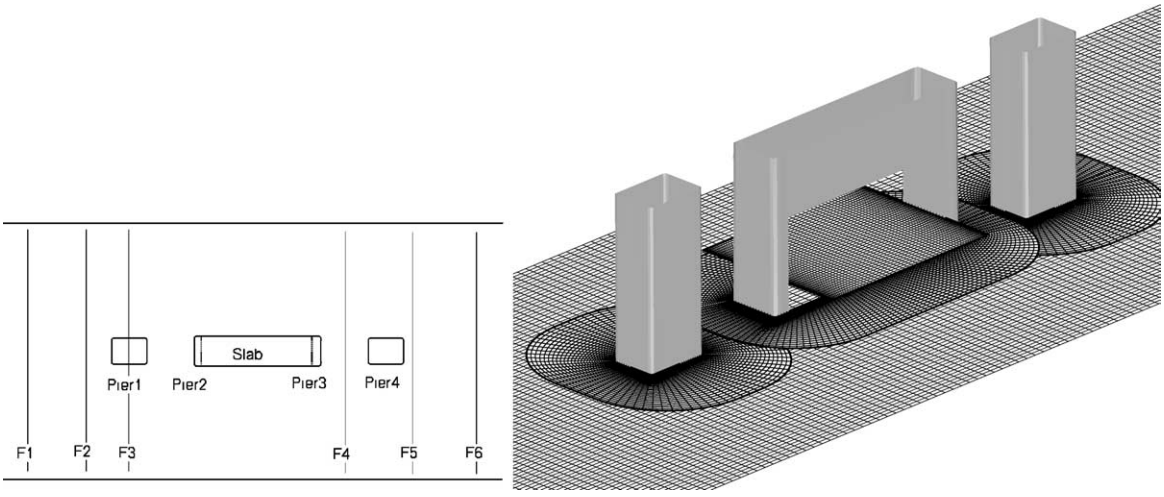

Fig. 1. Geometry of multiple piers, overset grid layout and measurement locations.

curvilinear coordinates in strong conservation form. The governing equations are discretized in space using the three-point, central, second-order accurate, finite-volume scheme. Third-order, fourth-difference, matrix-valued artificial dissipation terms (Lin and Sotiropoulos, 1997) are explicitly added to the discrete equations to suppress grid-scale oscillations. The discrete equations are integrated in time using a second-order-accurate, dual- or pseudo-time-stepping, artificial compressibility scheme. We integrate the equations in pseudo-time using the Beam-and-Warming approximate-factorization scheme in conjunction with V-cycle multigrid and local-pseudo-time-stepping for faster convergence. Non-reflecting, characteristic-based boundary conditions (Thompson, 1990) were applied at the outlet boundary to allow vortical structures to exit the flow domain without distortion. Arbitrarily complex geometries are simulated using a domain decomposition method with overset (Chimera) grids (Tang et al., 2003). Typically 25 pseudo-iterations were required to reduce all residuals by three orders of magnitude.

3. Flow past a bundle of wall-mounted rectangular piers

In this section, we employ the standard, high Reynolds number k–ε model to carry out a URANS simulation of the flow around a bundle of rectangular piers whose geometry is that of the actual foundation of a Chattahoochee River bridge (Georgia, USA). The actual foundation has four sets of piers that span the river. In this study, we simulate the flow around only one set as shown in Fig. 1. The computational domain is a $34b \times 14b$ rectangular domain, where b is the width of the first bridge pier (Pier 1 in Fig. 1). The water depth is $d = 4.16b$ and the river bed is assumed to be flat. Complex geometry is simulated with overset grids. As shown in Fig. 1, a background Cartesian grid is used to discretize the *empty* rectangular open channel and three O-type grids, tailored to resolve the geometrical features of the piers, are embedded within the background grid. The fact the rectangular slab connecting the two middle piers does not extend all the way to the bottom is accounted for by embedding a rectangular sub-domain just for this slab. Such an approach leads to a set of five, arbitrarily overlaid, structured sub-domains which give an approximate total of 10^6 active grid nodes. Calculations are carried out for $Re = 100{,}000$ based on the water depth and the bulk velocity at the inlet of the domain. The non-dimensional physical time step is $\Delta t = 0.25$. Fully-developed turbulent flow is specified at the inlet. The free-surface is treated as a flat rigid lid and extrapolation is used to specify boundary conditions for all flow variables at the outflow and lateral boundaries of the computational domain. The wall-functions approach is used to specify boundary conditions for the velocity components and the turbulence quantities at all solid walls. The URANS simulation is conducted for 5000 time steps to obtain a converged mean flow field.

Laboratory experiments for this flow were carried out in the Hydraulics laboratory at Georgia Tech using a 1:20 scale model. Model runs were conducted in flat-bed flume, and the bed was fixed and composed of sand with $d_{50} = 3.3$ mm (hydraulically fully rough regime). Mean velocity measurements were obtained using an acoustic Doppler velocimeter (ADV).

Fig. 2 shows instantaneous and time-average axial velocity contours on a horizontal plane just below the surface. The two snapshots (Fig. 2a, b) demonstrate the complex nature of the flow and show the large-scale instabilities of the shear layers emanating from the solid walls, which lead to asymmetric vortex shedding. It is important to note that large-scale unsteadiness and asymmetry develop naturally in our simulations, as the governing equations are iterated in time, without imposing any kind of explicit forcing on the approach flow. Also note that the vortices generated by the multiple piers are transported downstream, crossing boundaries of various overset grids smoothly without spurious distortions. Fig. 2c shows the time-average

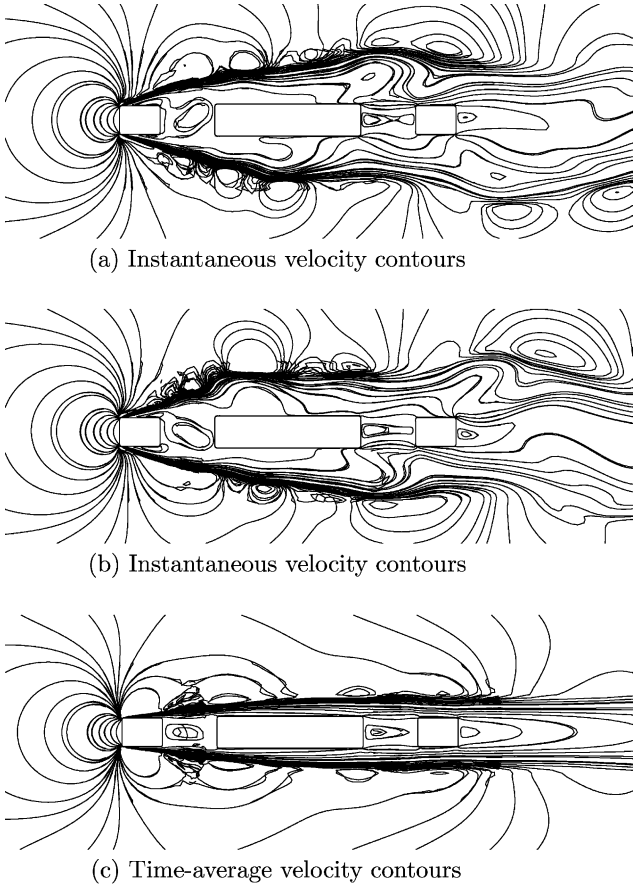

Fig. 2. Snapshots of resolved, (a) and (b), and time-averaged (c) streamwise velocity contours at a horizontal plane.

velocity field obtained by averaging the solution over the entire simulated interval (5000 time steps). As anticipated, the time-average flow is symmetric about the horizontal centerline and is characterized by shear-layers emanating from each pier and zones of reverse flow in the pier wakes.

The three-dimensional complexity of the instantaneous flow is shown in Fig. 3, which shows a snapshot of instantaneous particle paths around the piers. The instantaneous flow field is composed of an intricate web of horseshoe- and tornado-like vortices. Video animations show that these large-scale vortices appear and disappear periodically throughout the entire simulated time interval.

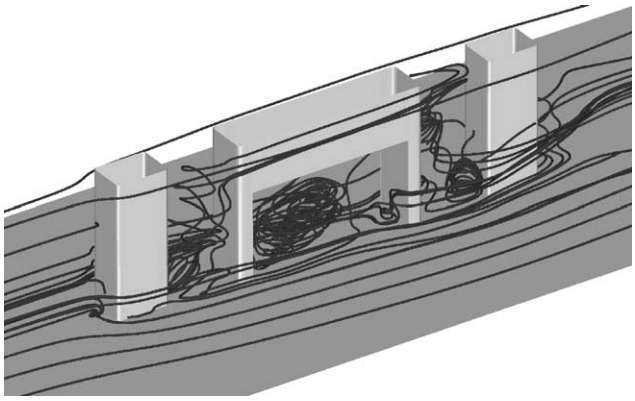

Fig. 3. Instantaneous three-dimensional streamtraces depicting large-scale vortical structures.

To validate our computations, we compare the simulated time-average streamwise velocity field with the experimental results. The comparisons are shown in Fig. 4, which depict time-average streamwise velocity profiles at three different planes that are perpendicular to the flow direction. The locations are shown in Fig. 1: plane F4 lies halfway between the last two piers; and planes F5 and F6 are downstream of the last bridge pier. On every plane, we compare the velocity profiles at three depths: $0.2d$, $0.4d$, and $0.6d$ measured from the bottom. As shown in these figures, our calculations capture all experimental trends with good accuracy. Such level of agreement between the computations and the measurements is particularly encouraging given the enormous complexity of the flow and the fact that the standard k–ε model was used for turbulence closure.

The agreement between our computations and the measurements is especially good in the wake of the four piers. This trend should be attributed to the fact that in this region the flow is dominated by the interactions of the upstream shed large-scale unsteady vortices, which are directly resolved in our simulation. Fig. 5 compares contours of resolved and modeled (time-averaged k predicted by the k–ε model) turbulence kinetic energy at one horizontal plane. As shown in the figure, the large-

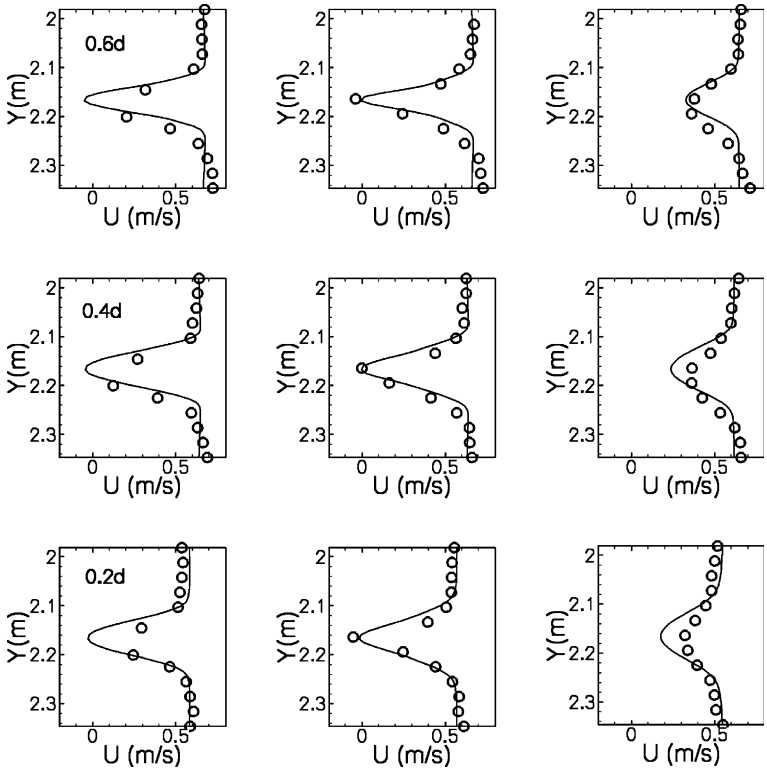

Fig. 4. Streamwise mean velocity profiles in the transverse direction at three depths at streamwise locations F4–F6 (— simulation; o experiment) (see Fig. 1 for plane locations).

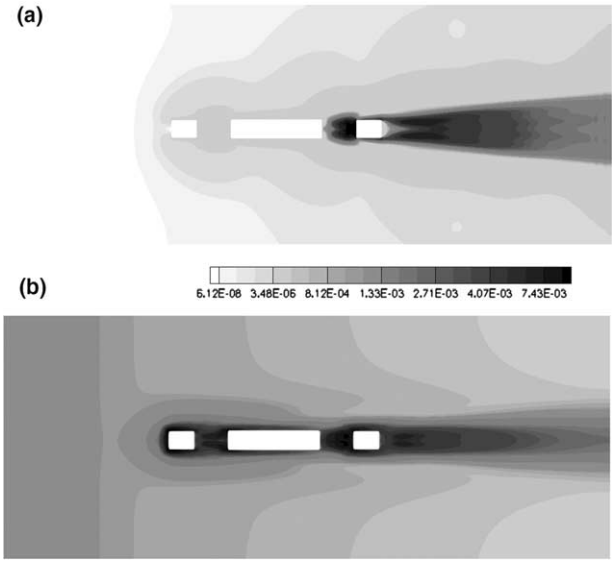

Fig. 5. Contours of resolved and modeled turbulence kinetic energy at a horizontal plane: (a) resolved by URANS simulation; (b) modeled by k–ε model.

scale structures in the flow account for most of the turbulence kinetic energy in the wake region while the turbulence model accounts for most of the energy upstream of the last pier.

4. Flow past a corner-mounted rectangular block

The geometry of the second test case consists of a rectangular block mounted in the junction region between the bottom and side walls of a rectangular open channel with a flat bed. The Re of 100,000 is based on the mean approach velocity and the length of the block L. The ratio of flow depth d to the obstacle length is $L/d = 5$. Two overset grids are used to discretize this geometry as shown in Fig. 6: a Cartesian background grid for the channel and a curvilinear, C-type grid for the region around the obstacle. The total number of active grid nodes in this overset grid layout is 900,000. The non-dimensional physical time step is $\Delta t = 0.025$. We carry out URANS with the one-equation Spalart–Allmaras model (URANS-SA) and DES with the standard DES-SA model. Therefore, in this case we seek to compare the predictive capabilities for URANS-SA and DES in a very complex, massively separated flow. Flow visualization experiments for this geometry have been reported by Chrisohoides and Sotiropoulos (2003) who developed a novel experimental technique for visualizing and extracting the time scales of coherent vortices at the free surface.

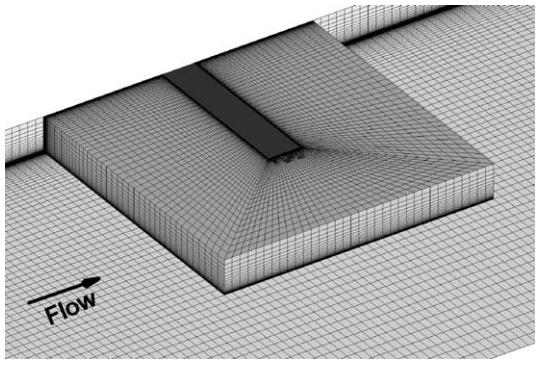

Fig. 6. Geometry of the corner-mounted rectangular block and overset grid system.

The general features of this flow as derived by our simulations and recent visualization experiments reported in Chrisohoides et al. (2003) and Chrisohoides and Sotiropoulos (2003) can be summarized as follows. As the upstream flow approaches the obstacle, it encounters a strong transverse pressure gradient that diverts it around the obstacle. A large region of recirculating flow forms at the upstream junction between the obstacle and the channel side wall. The flow within this upstream recirculating region is very complex consisting of multiple, large-scale eddies, which appear and disappear in a seemingly random manner. A slowly evolving, large recirculating zone is also present at the downstream end of the obstacle. A shear layer emanating from the edge of the obstacle develops at the interface between the slow moving fluid within this zone and the flow diverted around the obstacle. These complex features are illustrated in Fig. 7, which shows snapshots of instantaneous streamlines around the obstacle. The streamlines released inside the upstream recirculation zone suggest that the flow in this region is

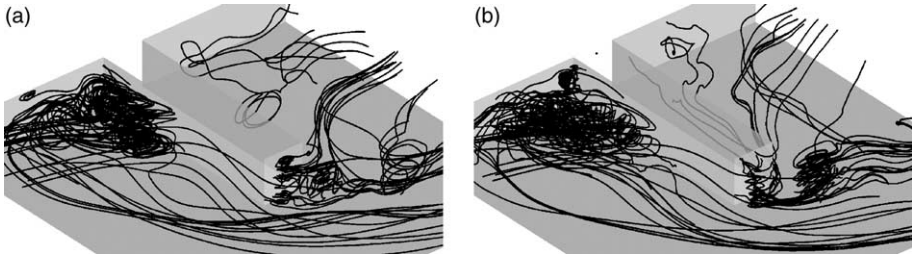

Fig. 7. Two snapshots of instantaneous three-dimensional streamtraces depicting complex vortical structures around the block.

dominated by an intricate web of highly three-dimensional and unsteady vortical structures. The figure also shows the unsteady roll up of the obstacle shear layer, the shedding of vortices, and the transport of these vortices downstream where they catch up and merge with previously shed vortices to form larger vortical structures.

As discussed above, Chrisohoides and Sotiropoulos (2003) showed that the flow in the upstream recirculation zone consists of multiple, large-scale eddies with very rich dynamics. The number and structure of these eddies vary continuously in time. There are instants in time when a single eddy occupies the center of the upstream recirculating zone. This eddy was shown to split into two eddies, which are rotated by the flow in the counter-clockwise direction, merge to form a larger eddy, and subsequently could bifurcate again to form two or more eddies. These complex processes were found to emerge repeatedly in a random manner. Chrisohoides and Sotiropoulos (2003) also showed that the upstream corner of the upstream recirculating zone exhibits similar rich dynamics with multiple smaller-scale eddies appearing and disappearing randomly. Representative snapshots of the visualized and simulated instantaneous coherent eddies in the upstream recirculating region are shown in Fig. 8.

To facilitate the comparisons between the visualized and simulated flow patterns it is important to stress that

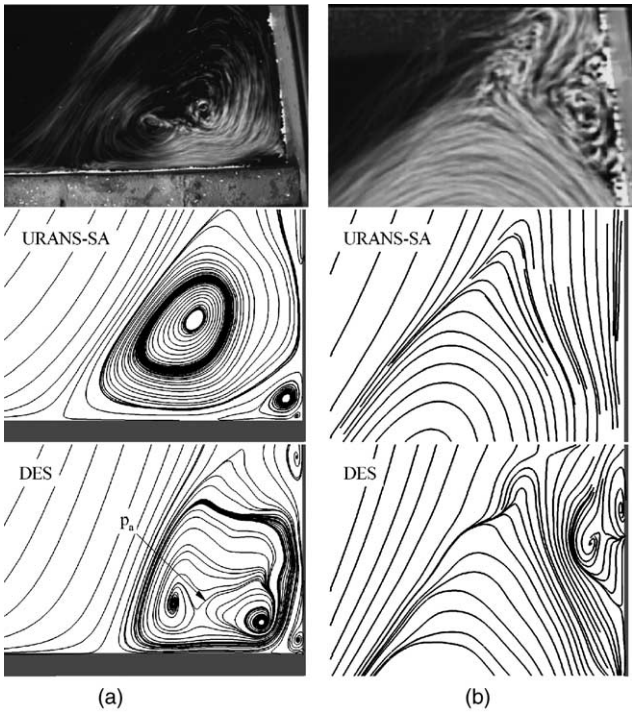

Fig. 8. Visualized (Chrisohoides and Sotiropoulos, 2003) and predicted streamline snapshot in the upstream separation region: (a) near the junction of the obstacle wall with the side of the channel and (b) upstream corner of the separation region.

the experimental images in Fig. 8 are not instantaneous flow visualization snapshots. They have rather been constructed by averaging digitally recorded light intensity time-series at each pixel of the image over a finite-size temporal window. Therefore, as discussed in detail in Chrisohoides and Sotiropoulos (2003), images such as those shown in Fig. 8 visualize the Lagrangian dynamics of coherent vortices at the time-scale of the averaging window. Since on the relatively coarse mesh we employ in our simulations both URANS and DES resolve only the large-scale dynamics of the flow, we argue that snapshots of surface streamlines constructed using the resolved velocity field should provide a reasonable approximation to the experimental visualization images constructed using the technique of Chrisohoides and Sotiropoulos (2003).

As shown in Fig. 8, the DES resolved flow field exhibits streamline patterns that are in good agreement with the experimental images. Video animations depicting the temporal evolution of resolved streamlines further show that the resolved DES field exhibits essentially the same rich dynamics observed in the experiment, with the eddies rotating, merging, and splitting continuously. On the other hand, the URANS simulation predicts a quasi-steady resolved flow field in this region. The resolved URANS recirculating zones consists of a single large eddy at all times, which undergoes mild temporal pulsations without exhibiting the experimentally observed eddy-splitting phenomena. Similar conclusions can be drawn from Fig. 9, which compares calculated snapshots of resolved large-scale vortex shedding from the obstacle shear layer with the visualization images of Chrisohoides et al. (2003). Clearly the DES simulation yields a resolved shear layer with much richer dynamics than that obtained by URANS, capturing more of the small-scale, high frequency content of the Kelvin–Helmoltz instability.

A rather remarkable feature of this flow qualitatively observed by Chrisohoides et al. (2003) is that it is characterized by regions of disparate time scales, such as the slowly evolving upstream and downstream recirculating regions and the unstable shear layer, which is dominated by high-frequency vortex shedding. The disparity of time scales and richness of dynamics in various regions of this flow are illustrated in Fig. 10, which shows time histories of the streamwise velocity component computed by DES at a point p_a located in the upstream recirculating region and a point p_b located within the shear layer (see Figs. 8 and 9 for point locations). The large differences in the temporal richness of the URANS and DES flow fields are further underscored in Fig. 11, which shows power spectrum distributions of the streamwise velocity components computed both by URANS-SA and DES at the same two points. In accordance with our previous discussion, in the upstream recirculating region URANS-SA yields

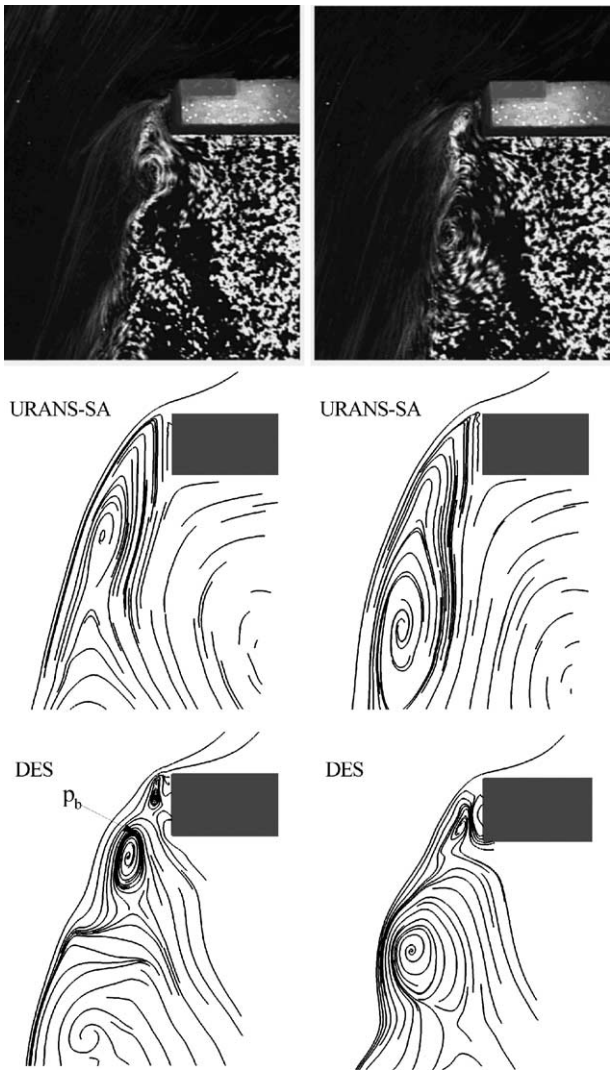

Fig. 9. Snapshots of visualized (Chrisohoides et al., 2003) and calculated streamlines using URANS-SA and DES in the shear layer.

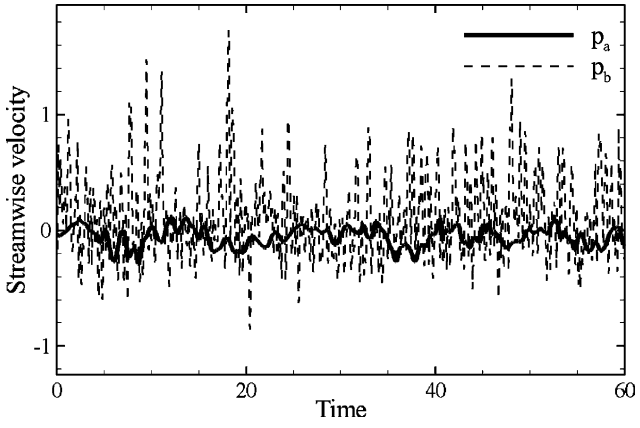

Fig. 10. Time series of computed streamwise velocity components at two selected locations (see Figs. 8 and 9 for point locations).

an essentially steady large-scale flow while the DES yields a clearly defined low frequency peak of considerable power. Within the shear layer, the URANS-SA yields unsteadiness whose intensity is significantly lower than that predicted by the DES. It is, however, worth noting from this figure that both the DES and URANS predictions agree well insofar as the location of the major peaks are concerned.

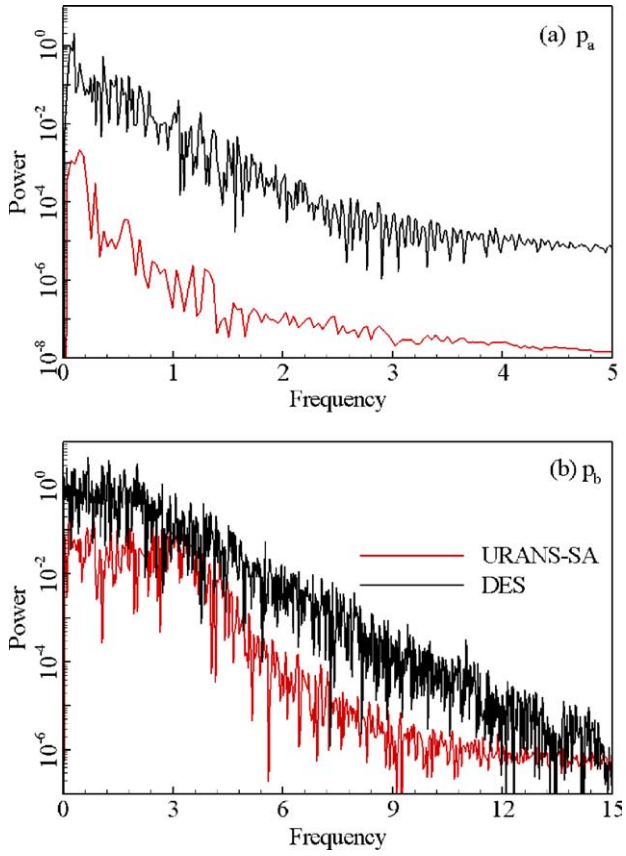

Fig. 11. Power spectrum distribution of computed streamwise velocity components at two selected locations of (a) point p_a and (b) point p_b (see Figs. 8 and 9 for point locations).

In spite of the qualitative nature of the comparisons shown in this section, the computed results underscore the superior performance of DES, at least relative to the specific URANS model, in resolving on relatively coarse meshes very rich large-scale dynamics both near the shear layer just downstream of the obstacle edge and inside recirculating regions. These results further demonstrate the need for detailed quantitative flow measurements if a more comprehensive assessment of the performance of the various modeling strategies is to be carried out for this flow.

5. Flow in a strongly curved rectangular bend

In this section we consider turbulent flow in a strongly curved, 90° duct. The cross-section of the duct is rectangular with a 6:1 height-to-width aspect ratio. Detailed experiments for this flow were conducted by

Kim and Patel (1994) who reported mean flow and turbulence statistics measurements for $Re = 2.24 \times 10^5$ based on the duct width H and the mean bulk velocity. This flow has served as a standard test case in ERCOFTAC workshops and has also been studied numerically by Sotiropoulos and Ventikos (1998) who employed a variety of linear and non-linear, steady RANS turbulence models. The computations of Sotiropoulos and Ventikos (1998) showed that the turbulence statistics near the inner (convex) wall of the bend are predicted reasonably well but the turbulence intensities near the outer (concave) wall are drastically underpredicted. Sotiropoulos and Ventikos (1998) attributed this trend to the well known inability of steady RANS models to account for the destabilizing effects of concave curvature at least not without explicit curvature corrections (see also discussion in Patel and Sotiropoulos (1997)). Experiments with turbulent boundary layers exposed to concave curvature (Barlow and Johnston, 1988), however, have revealed the growth of large-scale, unsteady, coherent vortical structures inside the boundary layer and have shown that these deterministic flow structures account for a considerable portion of the total production of turbulence kinetic energy. The precise nature of these vortical structures—i.e. whether they are coherent Görtler vortices as in laminar flows or large-scale vortical roles of finite streamwise extent—is still in dispute (Patel and Sotiropoulos, 1997). Nevertheless, the fact that large-scale, slowly varying flow structures appear to be an inherent feature of concave wall boundary layers raises the intriguing possibility that the presence of such structures could be predicted with unsteady statistical turbulence models. The computations reported in this section provide evidence in support of this assertion.

The computational domain starts $3.5H$ upstream from the inlet of the bend and extends up to $7.5H$ downstream from the exit of the bend (see Fig. 12). We discretize the entire duct cross-section (without invoking any symmetry assumptions) using two grid densities to investigate the sensitivity of the computed solutions to grid refinement: a coarse grid (CG) with 1.3×10^6 nodes and a fine grid (FG) with 3.1×10^6 nodes ($145 \times 69 \times 133$ and $197 \times 69 \times 229$ nodes in the streamwise, radial and normal directions, respectively). For both grids, the first grid node off the wall was located at $y^+ = 0.75$ almost everywhere. The computation was initialized with the results from a steady RANS simulation carried out using the SA model for turbulence closure. The SA model was also used for the URANS simulation (URANS-SA) and the DES (DES-SA).

All results reported herein were obtained by forcing the mean flow at the inlet plane with a broadband, random forcing generated using the random flow generation (RFG) technique of Smirnov et al. (2001). The RFG technique generates pseudo-turbulent inflow conditions based on a prescribed mean flow and Reynolds-stress tensor, which in this case were obtained from the experimental measurements of Kim and Patel (1994). It is important to clarify the rationale for prescribing pseudo-turbulent inflow conditions in this case. Unlike in direct numerical simulations and/or highly resolved LES, where temporally varying and spatially correlated inflow conditions are critical for accurate simulations, neither the URANS nor the relatively coarse-mesh DES we carry out in this work can respond to the broad range of scales introduced at the inlet via the RFG technique. Instead, the RFG technique provides a rational—albeit certainly not unique—way to perturb the base flow and explore whether out of the broad range of frequencies imposed at the inlet, the concave wall boundary layer will selectively amplify and become unstable to certain low frequency modes (see Fig. 17). Furthermore, since the perturbation field is based on the measured Reynolds stress field, the forcing is primarily imposed within the wall boundary layers where disturbances are also more likely to originate in the experiment. As we will subsequently show, imposing the RFG forcing is critical prerequisite for exciting and sustaining unstable modes inside the concave wall boundary layer, regardless of the specific turbulence closure model employed. URANS and DES simulations without impos-

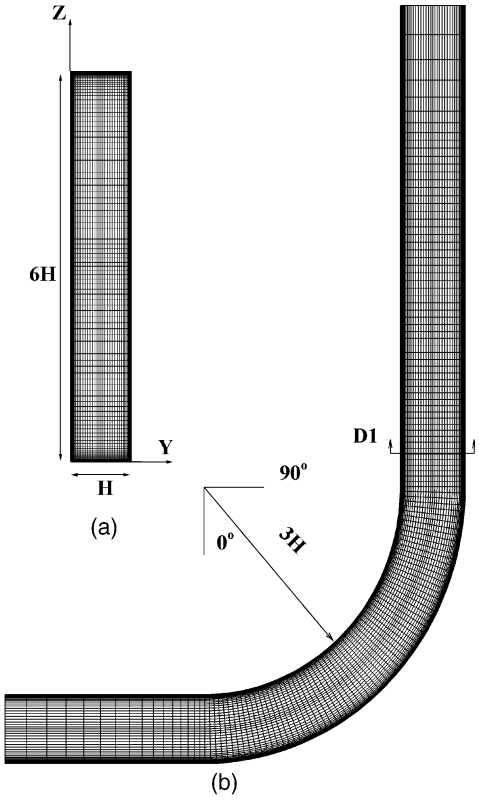

Fig. 12. Computational mesh and coordinates for the curved rectangular duct of Kim and Patel (1994): (a) cross-sectional view; (b) plane view.

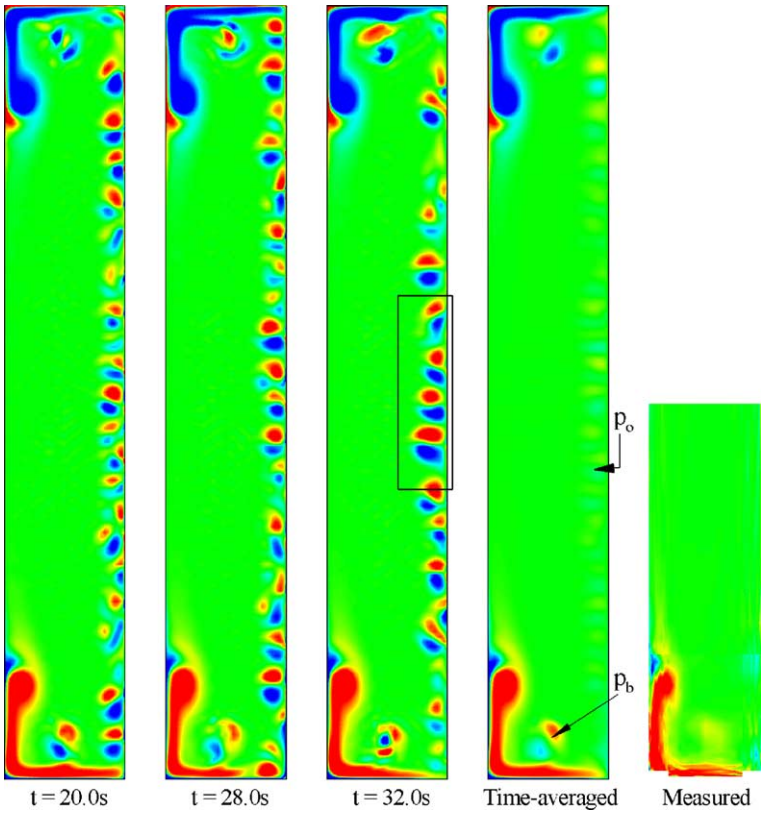

Fig. 13. Computed (DES) instantaneous (first three) and time-averaged, and measured time-averaged (Kim and Patel, 1994) contours of streamwise vorticity at station D1.

ing inlet forcing converge to a steady state solution, which is broadly similar to that obtained via the steady RANS model.

Fig. 13 shows instantaneous snapshots and the time-averaged distribution of the streamwise vorticity field at station D1 (see Fig. 12) calculated with DES along with the measurements of Kim and Patel (1994). Even though not included herein due to space limitation, the URANS simulations also exhibit, at least in a qualitative sense, the same general features as those observed in Fig. 13. It is readily apparent from this figure that the unsteady forcing at the inlet has only a small effect on the flow near the inner wall, which at all times remains essentially similar to its steady-state structure and in good overall agreement with the mean measurements of Kim and Patel (1994). The inlet forcing, however, drastically alters the structure of the flow on the outer (concave) side of the bend with highly unsteady, vortical structures emerging inside the concave wall boundary layer. The mushroom-like structure of the streamwise velocity contours and the cross-flow vectors shown in Fig. 14 reveal pairs of counter-rotating vortical structures with common flow away from the wall. The three-dimensional structure of these vortices is illustrated in Fig. 15, which shows a snapshot of two iso-surfaces of streamwise vorticity. As shown in this figure and further clarified in video animations of these iso-surfaces,

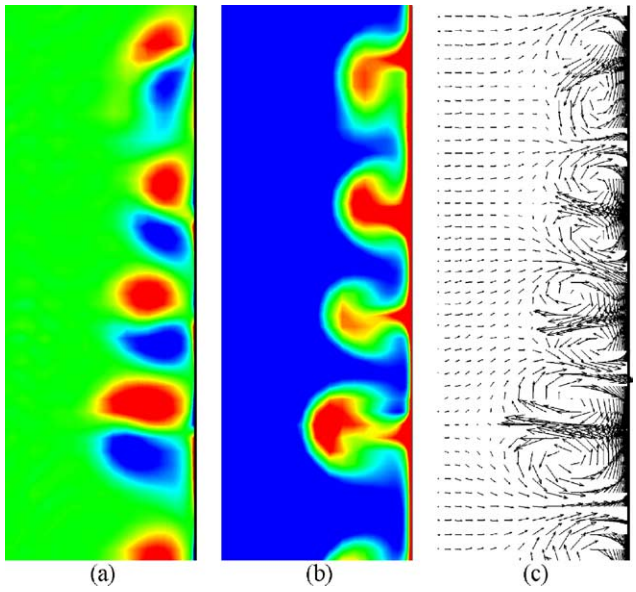

Fig. 14. Computed (DES) instantaneous streamwise vorticity (a) and streamwise velocity (b) contours, and secondary velocity vectors (c) at a selected region inside the outer wall at station D1 (see the rectangular box in Fig. 13 for the location).

streamwise structures begin to grow along the concave wall approximately half way through the bend. They are organized in pairs of opposite sign vorticity, meander in

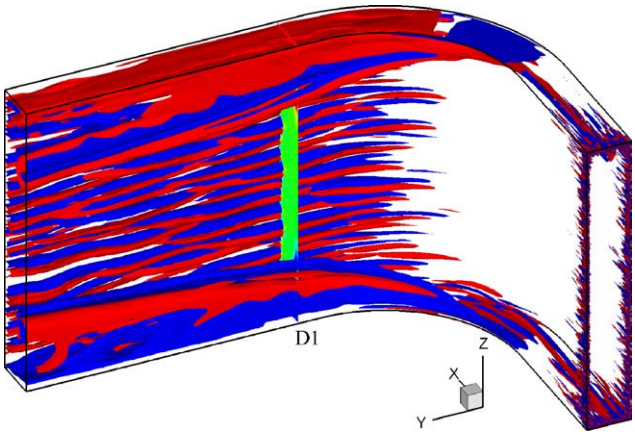

Fig. 15. Calculated (DES) positive (red) and negative (blue) iso-surfaces of instantaneous streamwise vorticity. (For interpretation of the references in color in this figure legend, the reader is referred to the web version of this article.)

space, and appear to have only limited streamwise coherence. Thus, the picture that emerges from our simulations is broadly consistent with the experimental findings of Barlow and Johnston (1988) who documented the growth of what they referred to as "*roll cells*" (instead of coherent Taylor–Görtler-like vortices) in concave wall boundary layers.

An important issue concerning the structure of the concave wall instability is whether or not the vortical rolls tend to orient themselves preferentially in the spanwise direction. The streamwise vorticity snapshots shown in Fig. 13 appear to suggest a rather random distribution in space and time. The time-averaged vorticity field also shown in Fig. 13, however, contains weak traces of regions of concentrated streamwise vorticity, which would tend to support the notion that the vortical rolls may in fact have some preference in their spanwise locations. Further evidence of such preferential spanwise spacing is shown in Fig. 16, which compares measured and predicted skin-friction profiles along the circumference of the duct at station D1—starting from the plane of symmetry and along the inner, bottom, and outer walls of the bend. Computed results include those obtained with DES, URANS on both the coarse and fine grids as well as the results from the steady RANS simulation. All computed results capture the general measured trends along the duct circumference but appear to consistently overpredict the skin-friction, especially near the junction of the inner and the bottom walls ($2 < S < 3$ in Fig. 16). The reason for this persistent discrepancy, which has also been reported in the steady RANS simulations of Sotiropoulos and Ventikos (1998), is not entirely clear. One possible explanation could be the different approaches adopted in the experiment and in the simulations for determining the wall shear stress (see Sotiropoulos and Patel, 1995, for a detailed discussion)—the experiments employed Preston tubes, which rely on the law-of-wall, while in the simulations the skin-friction was obtained via direct computation of the velocity gradient at the wall. Along the concave wall the measurements exhibit a clear, albeit weak, spanwise modulation, which is broadly consistent with the presence of pairs of mean streamwise vortical structures and provides some evidence that vortical rolls such as those found in our simulations were also present in the experiment of Kim and Patel (1994). This experimental feature is not captured by the steady RANS simulation but it is well reproduced, at least in a qualitative sense, by both the DES and URANS computations on both the coarse and fine grids. In fact as the mesh is refined both the DES and URANS simulations yield elevated levels of shear-stress, which tend to approach the measured skin-friction levels. It is also worth noting that the peaks and troughs in the calculated skin-friction distribution by DES-FG and URANS-FG correlate well with each other, which would tend to suggest that the number and spanwise spacing of the computed vortical structures is in close agreement in both simulations.

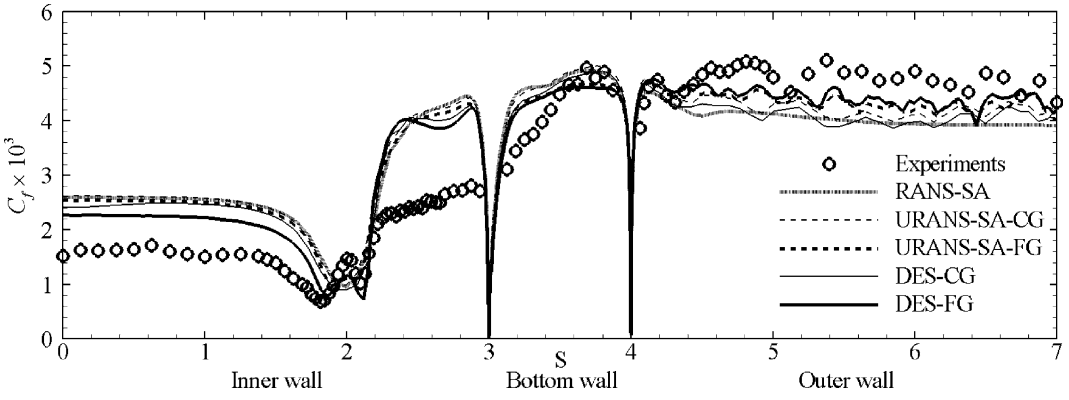

Fig. 16. Measured and computed time-averaged skin friction profiles at station D1 along the circumference of the duct. S is the arc length measured along the duct cross-section starting from the symmetry plane at the inner wall.

Fig. 17 compares the power spectra of the streamwise velocity component computed by DES and URANS-SA models at two points located inside the bottom wall and the concave wall boundary layers at station D1 (see also Fig. 13 for point locations). The low frequency peak in the power spectra at point p_b is due to weak unsteady modes in this region, which are excited by the interaction of the two counter-rotating vortices that evolved from the contraction induced vortex pair at the duct inlet in the experimental apparatus (see Kim and Patel, 1994, for details). The presence of these vortices was accounted for in the simulations since the measurements were used to specify inlet conditions (see Fig. 15). As shown in the snapshots of streamwise vorticity shown in Fig. 13, the excited unsteadiness in this region is characterized by unsteady pulsations of the vortex pair, periodic roll-up of the regions of vorticity of one sign around vorticity of opposite sign, and interactions with wall generated vorticity. In stark contrast to the inner wall, the growth of vortical rolls inside the centrifugally unstable outer wall boundary layer excites unsteady modes whose magnitude of power spectrum is more than one order of magnitude higher than those excited elsewhere in the flow. The spectrum distribution is concentrated in the low frequency regime with a distinct dominant frequency and several harmonics. The dominant frequencies computed by URANS-SA and DES both on the coarse and the fine grids are in the range of 0.05–0.1. Although power spectra predicted by DES and URANS-SA models show different magnitudes—with the DES in general predicting more intense unsteadiness—it is notable that the predicted frequencies are quite similar in this region. The dominant frequencies computed by URANS and DES on the fine grid, on the other hand, are approximately two times higher than those obtained on the coarse grid.

Measured and computed (RANS, DES, URANS) streamwise and radial mean velocity profiles on the coarse and fine meshes are compared with each other in Fig. 18 at three horizontal locations from the bottom wall ($z = 0.25$, 0.75, 3.0) at station D1. All computed results are in good overall agreement with each other and the measurements. Some small discrepancies are observed near the inner wall where the DES results capture the characteristic S-shaped structure of the streamwise velocity profiles at $Z = 0.75$ with somewhat better accuracy. Near the outer wall all simulations yield essentially indistinguishable results, which suggests that the onset of the concave wall instability has little effect on the mean velocity field. A dramatically different picture emerges, however, when we compare the calculated resolved turbulence kinetic energy profiles and the measured and computed total (modeled and resolved) primary Reynolds stress profiles at the same locations as those shown in Fig. 19. The profiles of resolved kinetic energy clearly show that with only exception near the

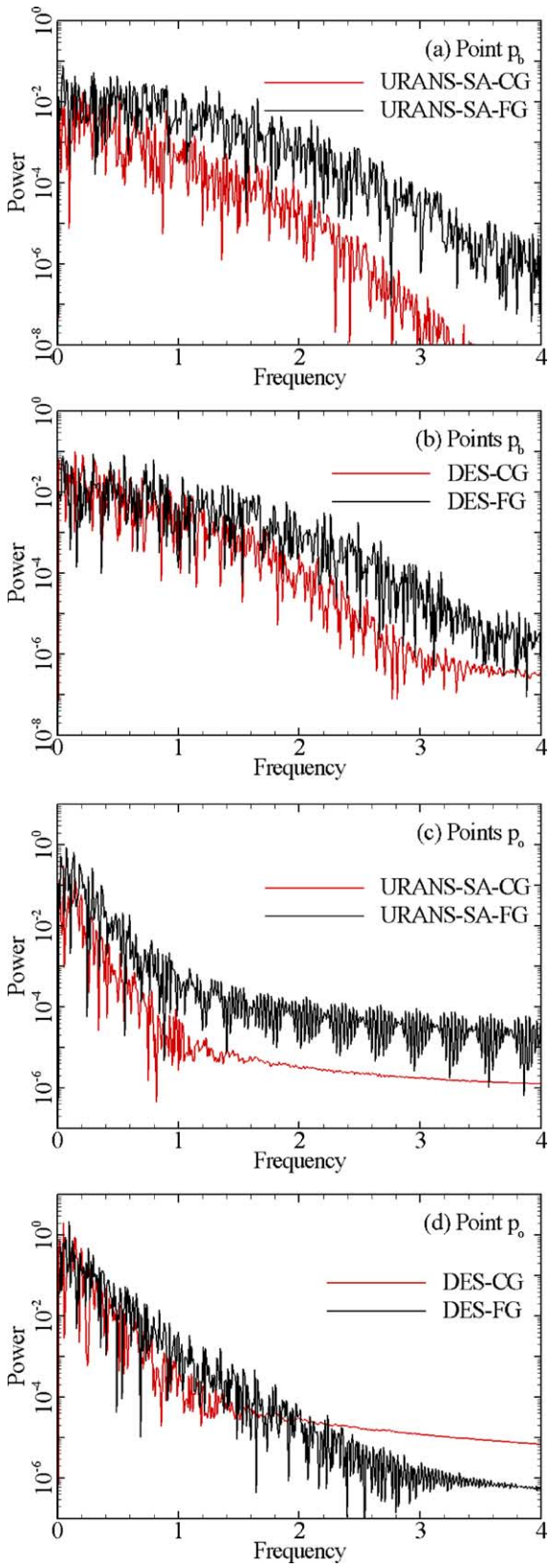

Fig. 17. Computed by URANS and DES on the coarse (CG) and fine (FG) grids power spectra of instantaneous streamwise velocity component inside the bottom (point p_b) and the outer (point p_o) wall boundary layers at station D1 (see Fig. 13 for points locations).

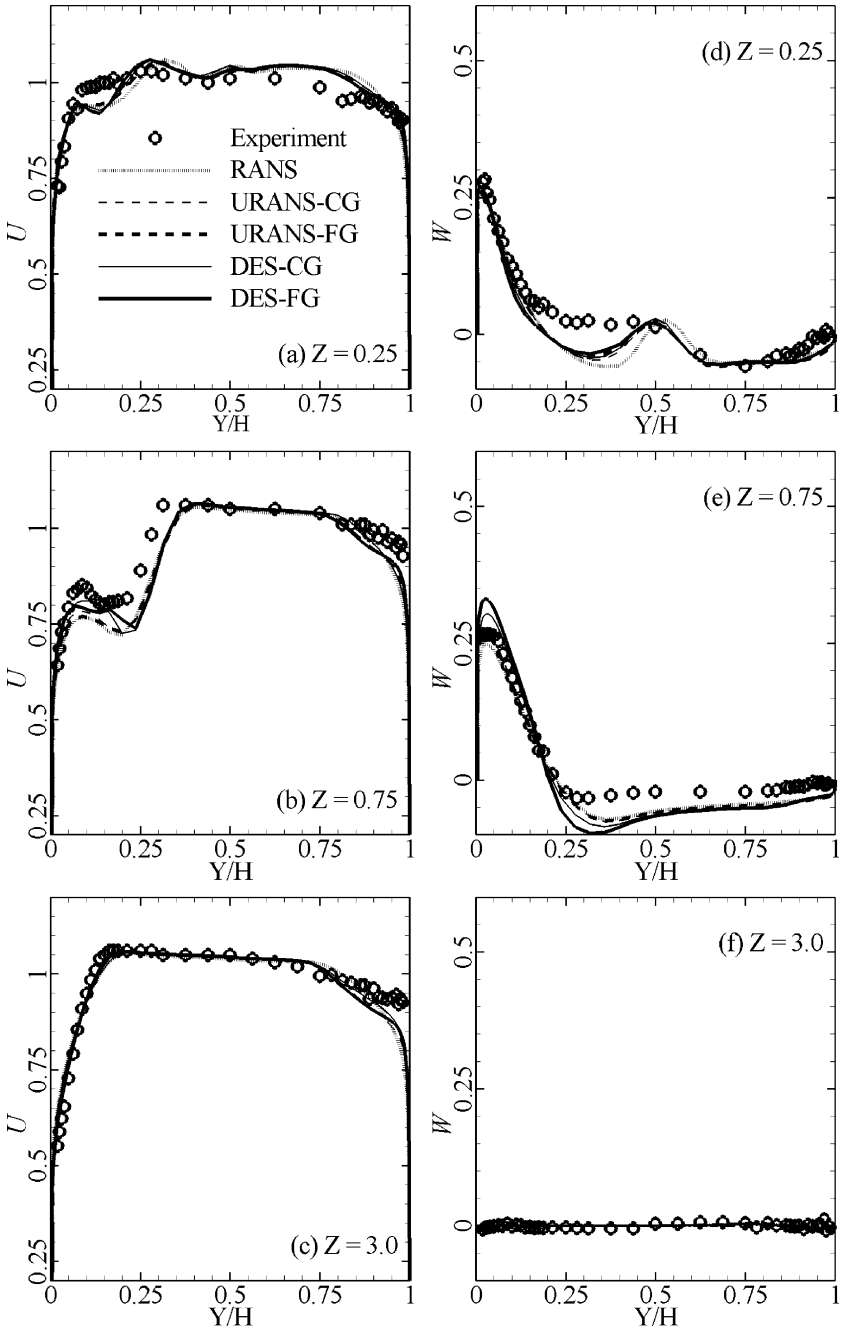

Fig. 18. Measured and computed by URANS and DES on the coarse (CG) and fine (FG) grids mean streamwise and vertical velocity profiles at station D1.

bottom of the cross-section (see profile at $Z = 0.25$), essentially no large-scale, unsteady modes are excited near the inner wall of the bend where the resolved energy is nearly zero. The spike in resolved kinetic energy near the center region of the cross-section at the $Z = 0.25$ plane is due to the low-frequency, weak, unsteady modes excited by the previously discussed interaction of the contraction induced streamwise vortex pairs at the inlet. It is interesting to note that on the same grid both URANS and DES yield identical resolved kinetic energy profiles in this region of the flow. This finding is in stark contrast with the effect of grid refinement and turbulence modeling strategy on the levels of resolved kinetic energy near the outer wall of the bend across the span of the cross-section. As the mesh is refined the levels of resolved energy near the concave wall increase significantly and this trend is considerably more pronounced in the DES than in the URANS simulation, which also yields the highest overall levels of resolved energy on both grid densities.

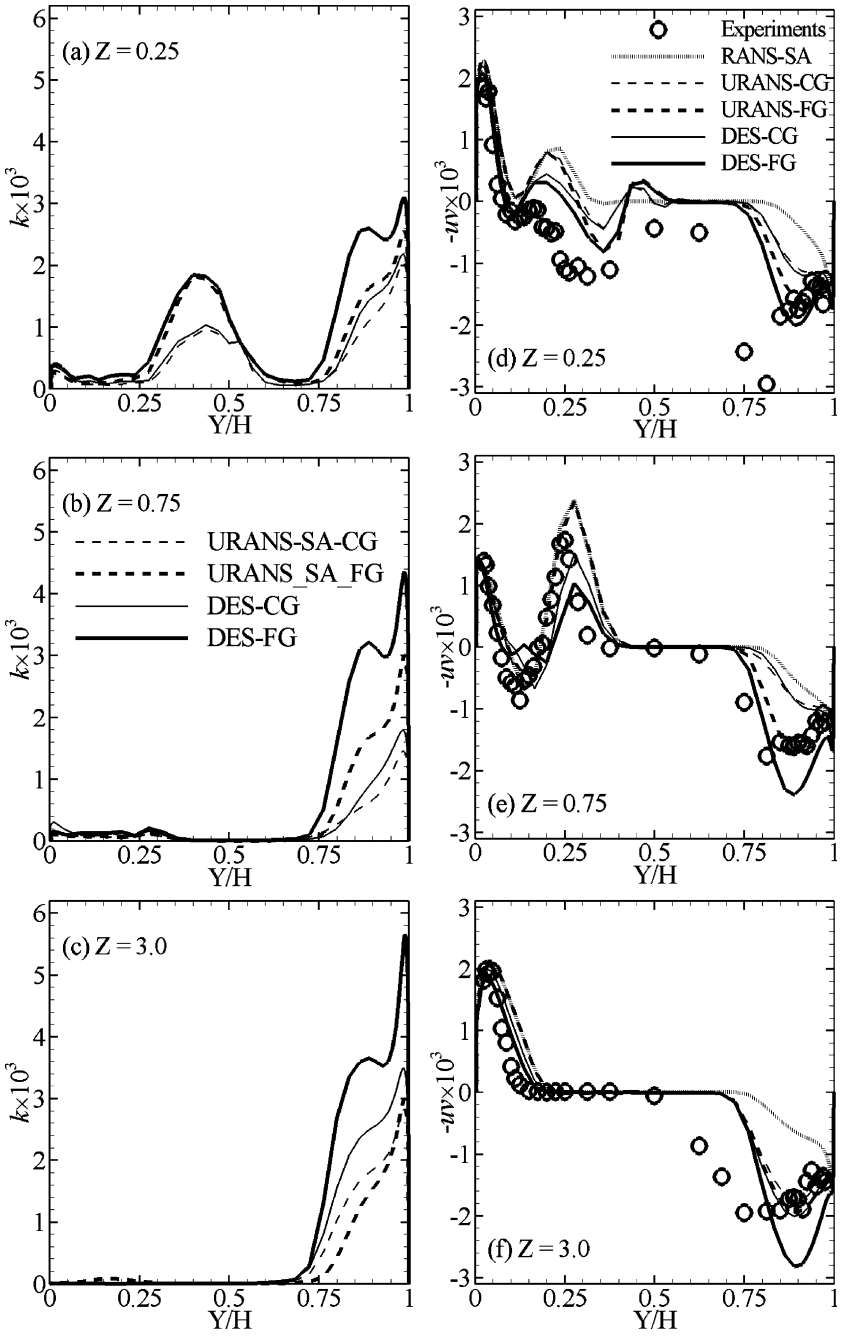

Fig. 19. Computed profiles of resolved turbulence kinetic engery and measured and computed profiles of total primary shear stress at station D1.

The dramatic effect of the onset of the concave wall instability on the structure of turbulence near the outer wall is further underscored in the comparisons of total primary Reynolds stress profiles. Near the inner wall of the bend all models yield very similar results, which are in reasonable overall agreement with the measurements. On the concave side of the bend, however, the steady RANS simulation grossly underpredicts the turbulent shear stress levels. The DES and URANS predictions, on the other hand, not only yield significantly higher Reynolds stress but also predict the peak in the profile to be closer to the location of the plateau in the experimental data. URANS on the fine mesh yields the best overall agreement with the experimental data while the DES is seen to considerably overpredict the level of turbulent stress especially on the fine mesh. In spite of the considerable improvement of the unsteady predictions over the steady RANS results, discrepancies with the measurements still persist. The layer of elevated shear stress near the outer wall is considerably thicker

and the peak stresses within this layer are higher in the experiment than in the simulations near the bottom of the cross-section.

To clarify the reasons for the considerable over-prediction by DES of the total turbulent shear stress near the outer wall as the grid is refined, we plot in Fig. 20 radial profiles of the modeled and the resolved contributions to the total shear stresses in the URANS and DES simulations at the plane of symmetry at station D1. As was also shown to be the case for the resolved kinetic energy in Fig. 19, the URANS and DES shear stress profiles on the coarse and the fine grids are essentially indistinguishable near the inner wall where the modeled contribution accounts entirely for the total turbulent stress. Near the outer wall the resolved stress by URANS, which accounts for approximately 70% of the total stress, is essentially unaffected by grid refinement and most of the improvement in the prediction of the total stress as the grid is refined comes from an increase in the modeled stress on the fine grid. For the DES, however, the resolved stress accounts for over 90% of the total stress and it is seen to increase by almost 50% as the grid is refined, a trend which accounts for the over-estimation of the total measured stress in this region. Even though one would anticipate that as the grid is refined in DES more of the modeled stress would be transferred to resolved stress (Spalart, 2000), the reason for the apparent large increase of the resolved stress is not clear and points to the need for further modeling refinements of the DES model.

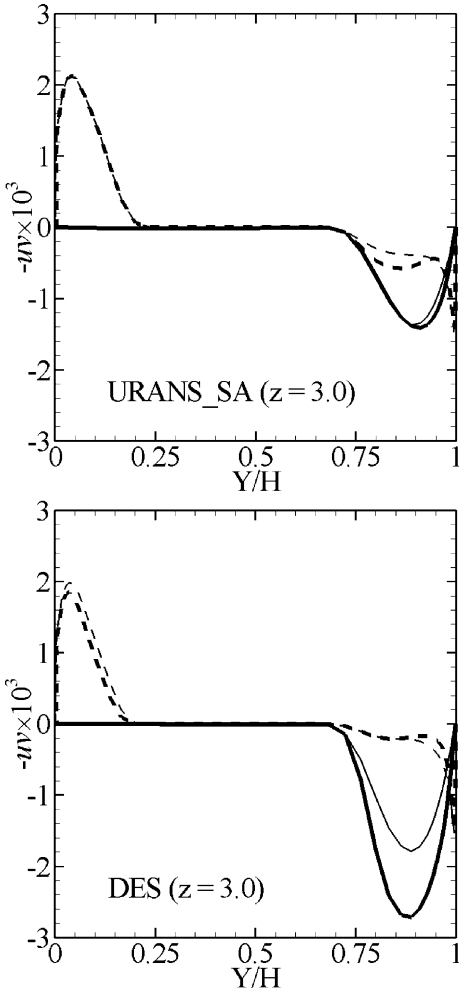

Fig. 20. Effect of grid refinement on modeled and resolved shear stress profiles at station D1. Solid line: Resolved; Dash line: Modeled; Thick line: Fine grid; Thin line: Coarse grid.

The results presented in this section show for the first time that the dramatic effect of concave wall curvature on the turbulence structure can be captured by exciting and resolving directly the large-scale, Taylor–Görtler vortical rolls without the need for introducing explicit curvature corrections in the turbulence model. The results shown in Figs. 16–19 along with the rich spatio-temporal dynamics of the flow within the concave wall boundary layer support the conclusion reached by Barlow and Johnston (1988), namely that "*...increases in turbulence intensities and Reynolds stresses across the outer layer are due almost entirely to increased energy in low-frequency, large-scale fluctuations...*" Clearly important discrepancies between computations and measurements near the outer wall of the bend still remain. One possible reason for these discrepancies could be the profound effect that upstream disturbances have been shown to have on the development of the concave wall instability and the ensuing turbulence structure (Barlow and Johnston, 1988). As was also concluded by Lund and Moin (1996), who carried out a LES of the Barlow and Johnston (1988) flow, it maybe very difficult if not impossible to accurately reproduce numerically a given set of experimental measurements for flow over a concave wall without precise information about the structure and intensity of inlet disturbances in the particular experiment.

6. Conclusions

We presented a numerical method for simulating complex 3D incompressible turbulent flows with unsteady statistical turbulence models. The potential of the method as a practical engineering simulation tool was illustrated by reporting results for three flows dominated by geometry-induced, unsteady coherent vortices.

Two of the simulated cases involved very complex geometrical features, which induced large-scale vortex formation and unsteady shedding. Our simulations showed that URANS even with relatively simple turbulence models (such as the standard k–ε model) can capture the unsteadiness and yield mean flow predictions in good agreement with measurements. We also showed, however, that unsteady statistical turbulence models can capture very complex, large-scale instabili-

ties of the mean flow such as the emergence of coherent, low-frequency vortical rolls inside the concave wall boundary layer in the curved bend case.

The promise of the DES approach relative to URANS simulations was illustrated for the flow past the corner-mounted block. The DES results successfully captured essentially all flow features observed in laboratory visualizations of this flow both in the upstream recirculating region and the shear-layer emanating from the sharp edge of the block. The URANS solution, on the other hand, yielded unsteadiness in the shear layer but failed to capture the very rich dynamics of the flow in the upstream recirculating region. Whether the failure of URANS in this case was due to the specific turbulence model employed (the Spalart–Allmaras model) remains to be investigated in a future study.

Both URANS and DES yielded promising results for the curved duct case. Our findings suggest an overall picture that is consistent with the experimental findings of Barlow and Johnston (1988) concerning the existence of large-scale, low frequency roll cells, which account almost entirely for the dramatic increases in turbulence energy near the concave wall. Our results also support the assertion of Patel and Sotiropoulos (1997) who argued that accurate predictions of concave curvature effects may require full 3D unsteady simulations with statistical turbulence models.

Acknowledgements

This work was supported by NSF Career grant 9875691, a grant from Georgia DOT, and a grant from Oak Ridge National Laboratory and DOE. We thank Terry W. Sturm for providing the experimental data for the first test case.

References

Barlow, R.S., Johnston, J.P., 1988. Structure of turbulent boundary layer on a concave surface. J. Fluid Mech. 191, 137–176.

Chrisohoides, A., Sotiropoulos, F., 2003. An experimental technique for visualizing lagrangian coherent structures in aperiodic flows. Phys. Fluids 15 (3), 25–28.

Chrisohoides, A., Sotiropoulos, F., Sturm, T., 2003. Coherent structures in flat-bed abutment flows: Computational fluid dynamics simulations and experiments. J. Hydr. Eng. 129 (3), 177–186.

Constantinescu, G.S., Chapelet, M.C., Squires, K.D., 2003. Turbulence modeling applied to flow over a sphere. AIAA J. 41, 1733–1742.

Durbin, P.A., 1995. Separated flow computations with the k–ε–v^2 model. AIAA J. 33, 659–664.

Hamed, A., Basu, D., Das, K., 2003. Detached eddy simulations of supersonic flow over cavity. AIAA paper 2003-0549.

Hedges, L.S., Travin, A.K., Spalart, P.R., 2002. Detached-eddy simulations over a simplified landing gear. J. Fluids Eng. 124, 413–423.

Iaccarino, G., Ooi, A., Durbin, P.A., Behnia, M., 2003. Reynolds averaged simulation of unsteady separated flow. Int. J. Heat Fluid Flow 24, 147–156.

Kim, W.J., Patel, V.C., 1994. Origin and decay of longitudinal vortices developing in a curved rectangular duct. J. Fluids Eng. 116, 45–51.

Lin, F.B., Sotiropoulos, F., 1997. Assessment of artificial dissipation models for three-dimensional incompressible flow solutions. J. Fluids Eng. 119, 331–340.

Lund, T.S., Moin, P., 1996. Large-eddy simulation of a concave wall boundary layer. Int. J. Heat Fluid Flow 19, 290–295.

Morton, S.A., Steenman, M.B., Cummings, R.M., Forsythe, J.R., 2003. DES grid resolution issues for vortical flows on a delta wing and an F-18C. AIAA paper 2003-1103.

Patel, V.C., Sotiropoulos, F., 1997. Longitudinal curvature effects in turbulent boundary layers. Prog. Aerospace Sci. 33, 1–70.

Schmidt, S., Thiele, F., 2002. Comparison of numerical methods applied to the flow over wall-mounted cubes. Int. J. Heat Fluid Flow 23, 330–339.

Smirnov, A., Shi, S., Celik, I., 2001. Random flow generation technique for large eddy simulations and particle dynamics modeling. J. Fluids Eng. 123, 359–371.

Sotiropoulos, F., Patel, V.C., 1995. On the role of turbulence anisotropy and near-wall modeling in predicting complex, 3D, shear flows. AIAA J. 33, 504–514.

Sotiropoulos, F., Ventikos, Y., 1998. Prediction of flow through a 90° bend using linear and non-linear two-equation models. AIAA J. 36, 1256–1262.

Spalart, P.R., 2000. Strategies for turbulence modelling and simulations. Int. J. Heat Fluid Flow 21, 252–263.

Spalart, P.R., Allmaras, S.R., 1994. A one-equation turbulence model for aerodynamic flows. La Recherche Aerospatiale 1, 5–21.

Spalart, P.R., Jou, W.H., Strelets, M., Allmaras, S.R., 1997. Comments on the feasibility of LES for wings and on a hybrid RANS/LES approach. In: Liu, C., Liu, Z. (Eds.), First AFOSR International Conference on DNS/LES, August 4–8, Ruston, LA. In: Advances in DNS/LES. Greyden Press, Columbus, OH.

Squires, K.D., Forsythe, J.R., Morton, S.A., Strang, W.Z., Wurtzler, K.W., Tomaro, R.F., Grismer, M.J., Spalart, P.R., 2002. Progress on Detached-Eddy Simulation of massively separated flows. AIAA Paper 02-1021.

Strelets, M., 2001. Detached eddy simulation of massively separated flows. AIAA paper 2001-0879.

Tang, H.S., Jones, S.C., Sotiropoulos, F., 2003. An overset-grid method for 3D unsteady incompressible flows. J. Comp. Phys. 191, 567–600.

Thompson, K.W., 1990. Time-dependent boundary conditions for hyperbolic system, II. J. Comp. Phys. 89, 439–461.